Validation of Cryogenic Propellant Tank Self-Pressurization

Hong. Q. Yang *
CFD Research Corporation (Jacobs Space Exploration Group), NASA Marshall Space Flight Center, Huntsville, AL

Chintan S. Patel †
Qualis Corp (Jacobs Space Exploration Group), NASA Marshall Space Flight Center, Huntsville, AL

Brandon R. Williams ‡
NASA Marshall Space Flight Center, Huntsville, AL

NASA's near-future long-term space missions necessitate advancements in cryogenic fluid management (CFM), which includes safe and reliable long-term propellant storage. Consequently, NASA STMD (Space Technology Mission Directorate) has established the CFM Portfolio Project to improve CFM technologies for upcoming missions. As a part of CFM Modeling Portfolio, NASA Marshall Space Flight Center's (MSFC) Fluid Dynamics branch within the Propulsion Systems Department is tasked with assessing and improving computational tools used to support flight projects such as Human Lander System and Commercial Lunar Payload Services. One of the challenging modeling problems is that of self-pressurization of propellant tank due to heat leakage over long time periods. Reduced order and nodal tools find it extremely difficult to accurately predict self-pressurization under transient conditions or where complex flow patterns or thermal gradients exist, and application of 3-D CFD (computational fluid dynamics) simulations is necessary to characterize these problems. Until recently, CFD simulations for these long-term processes (order of hours or days) have been too impractical to conduct due to prohibitive wall time and computational resource requirements. The requisite CFD tool need to be efficient, computationally scalable, modular with ability to incorporate various physics models, and robust enough to not accumulate conservation errors over several hours of simulated time. NASA MSFC's Loci-Stream CFD tool along with the VOF module is a great candidate to fit this mold. In this paper, we validate Loci-Stream for predicting self-pressurization of a flight scale propellant tank so it can serve as a reliable design and analysis tool for NASA's CFM application needs. Liquid hydrogen tank pressurization tests carried out at the K-site testing facility provide a reliable data set for this purpose. These tests were simulated using Loci-Stream solver with VOF module as well as a hybrid approach which uses a lumped model for the ullage gas domain and CFD simulation of the liquid propellant. Both are shown to have very good predictive capabilities over multiple K-site experiments.

I. Nomenclature

A_{in}	=	Gas-liquid interface area
α	=	Thermal expansion coefficient
C_m	=	mass transfer coefficient (accommodation factor)
$_{cond}$	=	Subscript denotes condensation
dt	=	time step
e	=	Internal energy
$_{evap}$	=	Subscript denotes evaporation
F	=	Volume of fluid (liquid volume fraction in a control volume cell)
$\mathbf{G}$	=	gravitational force term in the momentum equation
$\mathbf{g}$	=	gravitational acceleration

*Chief Scientist, Fluid Dynamics Branch (ER42), NASA Marshall Space Flight Center (MSFC); AIAA Associate Fellow
†Computational Fluid Dynamicist, Fluid Dynamics Branch (ER42), NASA MSFC
‡Lead Aerospace Engineer - Fluid Mechanics, Fluid Dynamics Branch (ER42), NASA MSFC

$_g$ = Subscript denotes gas
h = Enthalpy
$_{in}$ = Subscript denotes gas-liquid interface
$_{i,j,k}$ = Subscripts denote spatial co-ordinates in Einstein notation
k = Thermal conductivity
κ = Iso-thermal compressibility
$_l$ = Subscript denotes liquid
$\dot{m}$ = Phase change mass transfer (evaporation/condensation) rate
p = fluid pressure
Φ = Heat dissipation through shear stress in total energy equation
R_g = Specific gas constant
ρ = density of fluid
$_{sat}$ = Subscript denotes saturation condition
T = Static temperature
t = Time
$\mathbf{u}$ = fluid velocity
V = Volume

Note: All vectors/tensors, except when using Einstein notation, are represented with **bold** font.

II. Introduction

Cryogenic propellants promise higher specific impulses than storable hypergolic fuels, but storage for long-duration missions must be demonstrated. Long-term in-space storage of cryogenic propellants including upper stages and potentially propellant depots is very important to meet the technological challenges of NASA's future exploration missions. One of the challenges in cryogenic fluid management (CFM) is that cryogenic propellant tanks in space are exposed to incident solar radiation, which heats the liquid in the tank over time. The increase in temperature results in an increase in pressure as the liquid cryogen vaporizes, i.e., self-pressurization.

During the time interval when the tank is 'locked up', heat transfer through the tank walls results in an energy increase in both the liquid and the ullage space vapor. Experience has shown that this energy increase is not uniformly distributed in either the liquid or vapor, but rather higher temperatures occur in the topmost layers of both the liquid and vapor regions due to natural convection in both 1-g and low-g conditions. This phenomenon is described as thermal stratification and has been reported by numerous observers [1–4] in early space programs. Associated with this temperature stratification is a rise in tank pressure due to a combination of heat transferred to the ullage vapor plus possible vaporization of a portion of the liquid. A means for predicting the amount of pressure rise as it varies with time and tank wall heat flux is needed in order to properly plan for propellant fluid management, to determine tank structural stresses, to determine tank venting requirements, and possibly to foresee the need for additional pressurant gas. The extent of liquid temperature rise, separate from its effect on the tank pressure, is also needed in order to determine the impact on pump performance. In addition, excessive temperatures can result in cavitation due to a reduction in Net Positive Suction Head (NPSH), thus either damaging the pump or adversely affecting the pump performance.

Numerous recent studies have focused on predicting the pressurization process in cryogenic propellant tanks [5–15] and have produced analytical, experimental, and numerical results. These studies play a critical role in the design of cryogenic storage systems since tank pressure must be controlled for long-duration space missions.

Due to the low boiling point of hydrogen and the low thermal conductivity of both the gas and liquid phase, it is possible for solar heating to result in the coexistence of subcooled liquid and superheated vapor within the same tank. When such a situation occurs, simple thermodynamic analysis cannot accurately predict the rate of pressure rise within the system. High-fidelity computational fluid dynamics (CFD) simulations will play an essential role in predicting the actual thermodynamics of pressurization. The objective of this study is to develop and validate a finite-volume-based CFD model to predict the thermal stratification and self-pressurization in a liquid hydrogen tank. The final goal is the development of technology required for the design of CFM systems to accomplish tasks such as liquid acquisition, thermal control of the cryogenic tank, and fluid transfer.

Unlike a typical CFD code, the computational tool for the CFM application requires multi-phase and multi-physics capability as tank pressurization involves both liquid and gas phases and their mutual interaction. At the same time, numerical modeling tools need to have sufficient fidelity to answer critical design and operational issues and must

be verified by comparing them with test data. Several well-established methods exist for dealing with interfaces in fluid flow. These methods include the front tracking [16], the level set method [17, 18], and the volume of fluid (VOF) methods [19, 20]. For CFM applications, ensuring mass conservation and energy conservation for both phases is critical. In these situations, VOF methods are found to be superior.

As part of NASA's CFM Modeling Portfolio goal of model validation, the Loci-Stream computational fluid dynamics (CFD) tool used by NASA MSFC is being validated for predictive accuracy in the relevant physics of cryogenic propellants during storage and mission operations. The principal aim of the work documented in this report is to validate the Loci-Stream CFD code and implemented physics models used for CFM and propellant tank dynamics applications. The physics under consideration is the self-pressurization of a tank containing cryogenic liquid and a single species ullage gas (i.e., does not contain non-condensable vapor). In the following sections, the experimental set-up, the Loci-Stream-VOF CFD code, a lumped gas CFD model and the essential features needed to deal with the heat and mass transfer are be described, and finally a comparison of the simulation results and experimental data are presented.

III. Test Description

A. K-site Testing Facilities

The experiments used for this validation study were performed in the K-site facility at NASA Glenn Research Center [21, 22]. The tank, in this case, was a flight-weight aluminum ellipsoidal enclosure with an internal volume of $4.95\,\mathrm{m}^3$. It was insulated with two multi-layer insulation (MLI) blankets. Figure 1 [21] shows the tank and its schematic. The facility consisted of a vacuum chamber enclosing a cylindrical cryo shroud whose temperatures can be maintained with electrical resistance heaters. Within the shroud, a liquid hydrogen (LH2) tank was suspended by twelve fiberglass composite struts. The tank was constructed from 2219 aluminum, with a wall thickness varying between 1.9558×10^{-3} m and 2.2098×10^{-3} m. The tank was fabricated by joining two halves of a 1.2/1.0 oblate spheroid to a 0.0381 m cylindrical section.

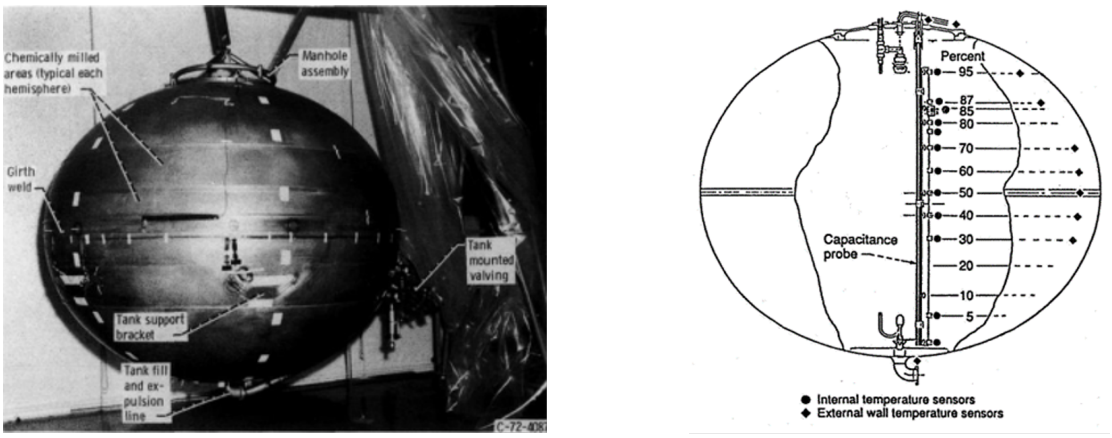

(a) Tank without MLI insulation **(b) Tank schematic**

Fig. 1 Liquid hydrogen tank tested at K-site

The experiments were conducted for the ellipsoidal LH2 tank at fill levels of 29%, 49%, and 83%, and wall heating levels of $2.0\,\mathrm{W/m}^2$ and $3.5\,\mathrm{W/m}^2$. The duration of the experiments was between 12 and 18 h. The tank had a volume of $4.89\,\mathrm{m}^3$ and was representative of a system that could be used in future vehicles. Pressure measurement devices and thermocouples were positioned at several vertical locations inside the tank and on the wall.

Before the self-pressurization experiments began, boil-off tests were performed to estimate the net heat leak into the LH2 tank. During these tests, the tank was 95% full of LH2, and the operating pressure was approximately 117 kPa. Heat leaking into the tank caused the liquid to evaporate, and the resulting boil-off was directed through volume flow meters. After the boil-off tests were performed, the tank was drained to the desired fill level, the operating pressure was reduced to 103 kPa, and venting occurred for another 4 h before tank lock-up. Finally, when lock-up occurred, the tank was allowed to self-pressurize for approximately 20 h.

B. Experimental Results

Figure 2 [22] shows the typical pressurization (2a), temperature histories at selected vertical locations (2b), and the vertical temperature profile (2c).

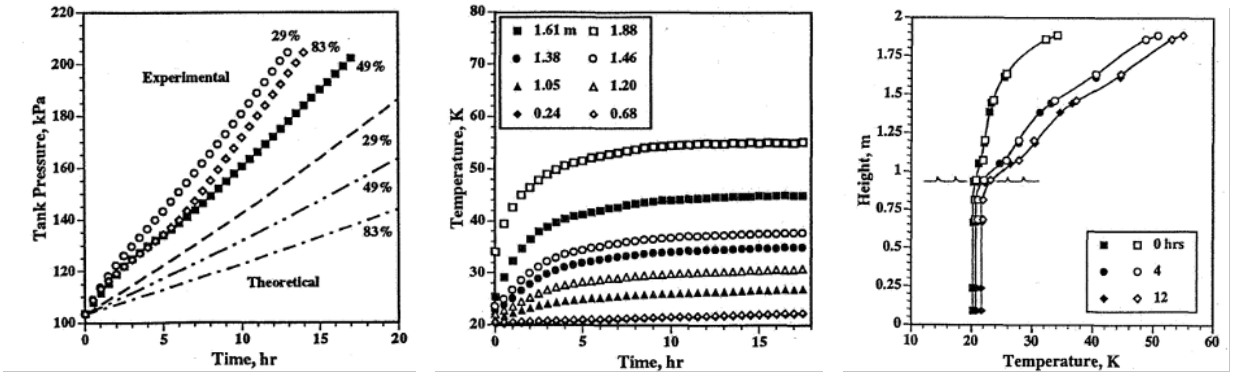

(a) Ullage pressure vs time history for $3.5\,\mathrm{W/m^2}$ **heat flux**

(b) Temperature at select vertical locations vs time

(c) Temperature profile across tank height at select times

Fig. 2 K-site experiment results for 29%, 49%, and 83% fill level

We observe that:

1) An initial transient took place over nearly 5 h before the linear increase in pressure (Figure 2a)
2) The role of the initial transient is to build up a stratified temperature field in the ullage (Figure 2b)
3) After the initial transient, pressurization is linear (Figure 2a)
4) After the initial transient, the contribution of mass transfer to pressurization is more than the contribution from sensible heating (Figure 2c)
5) Stratification of the temperature field in the ullage indicates that heat convection dominated heat conduction (Figure 2c)
6) The temperature in the liquid is almost uniform in the vertical direction with visible stratification near the gas-liquid interface (Figure 2c)

IV. Computational Model

The VOF method is a powerful and robust technique for simulating free-surface and gas-liquid interfacial flows such as those encountered in CFM. The geometric algorithms tracking the interface are more accurate than other methods at simulating free-surface flows and allow simulations with excellent conservation properties when adequately implemented. The Fluid Dynamics Branch (ER42) at Marshall Space Flight Center (MSFC) has been active in applying CFD methods to CFM analyses and tank dynamics applications, such as propellant slosh, to extract engineering metrics, like slosh damping, that can be used for system-level design and analysis.

In response to the limitations of commercial VOF tools and other multiphase methods at the time, NASA/MSFC established a path [23] to fulfill its simulation needs by developing a VOF module to augment the general-purpose CFD program Loci-Stream. Loci [24] is a novel software framework that has been applied to the simulations of non-equilibrium flows. The Loci system uses a rule-based approach to automatically assemble the numerical simulation components into a working solver. This technique enhances the flexibility of simulation tools, reducing the complexity of CFD software induced by various boundary conditions, complex geometries, and different physical models. Loci plays a central role in building flexible goal-adaptive algorithms that can quickly match numerical techniques with various physical modeling requirements. Loci-Stream [25][26] is a pressure-based, all-speed CFD code for generalized meshes in the Loci framework that has been applied and validated over a wide range of problems. Loci-Stream uses SIMPLE, SIMPLEC, and PISO algorithms for pressure-momentum coupling and provides various turbulence models which can be executed in Reynolds-Averaged Navier-Stokes (RANS) or Large Eddy Simulation (LES) mode. The coupled simulations between the flow solver and VOF transport are carried out using the Loci-Stream flow solver and an external VOF module [27]. The final product, Loci-Stream-VOF, has been applied to practical rocket propulsion-related

VOF applications and has shown significant parallel scalability, up to thousands of CPU cores [23–27].

While VOF is a high-fidelity model for capturing the evolution of a gas-liquid interface, the accuracy and generality come with a higher computational cost compared with other methods. For the long duration self-pressurization scenarios described above, that computational cost may become a significant disadvantage. Because the interface is essentially static, other methods where the gas and liquid domains are simulated in a segregated but coupled fashion are also possible. As part of this analysis, a model which treats the ullage as a single lumped gas node coupled to a CFD simulation of the liquid propellant is described and compared to the full fidelity VOF model.

A. Governing Equations

The governing equations for mass, momentum, and energy are given in the Equation 1, 2 and 3. These equations are for single-phase fluids and implemented in the Loci-Stream code [25, 26]. We will discuss the incorporation of two-phase fluids in the VOF Module section below, where these equations are accompanied by an additional transport equation for the volume of fluid.

$$\frac{\partial \rho}{\partial t} + \frac{\partial \rho u_j}{\partial x_j} = 0 \tag{1}$$

$$\frac{\partial \rho u_i}{\partial t} + \frac{\partial \rho u_j u_i}{\partial x_j} = \frac{\partial p}{\partial x_i} + \frac{\partial \tau_{ij}}{\partial x_j} + \mathbf{G} \tag{2}$$

$$\rho c_p \frac{DT}{Dt} = \alpha_l T \frac{Dp}{Dt} + \frac{\partial}{\partial x_i}(k \frac{\partial T}{\partial x_i}) + \Phi \tag{3}$$

Since the self-pressurization physics is buoyancy driven in the liquid phase in the presence of gravity, a Boussinesq approximation is invoked in the momentum equation for the buoyancy source term. The liquid density is assumed to be constant except for calculating the buoyancy force, where the liquid density is considered a linear function of temperature in the gravity term. Equation 4 defines the contribution to the body force in momentum equation, where ρ_{ref} is liquid density at the reference temperature T_{ref}.

$$\mathbf{G} = -\alpha_l \, \rho_{ref} \, (T - T_{ref}) \, \mathbf{g} \tag{4}$$

B. Energy Conservation

The energy equation conserves total energy of the system as described in Equation 5. In a previous study of constant density problems, the internal energy form, was used [5, 6]. Barsi and Kassemi [5, 6] presented a comprehensive review of the various constant density models, among which the CFD models were able to provide detailed simulations of tank pressure evolution for the current K-site experiments, together with two dimensional (2-D) and or 3-D depictions of the temperature and velocity fields. Using the internal energy form, Barsi and Kassemi [5] showed favorable agreements with the experimentally measured pressure histories. In this study, however, the conservation is imposed by an enthalpy-based formulation (Equation 3).

$$\rho \frac{De}{Dt} = \nabla(k \nabla T) - p \, \nabla \cdot \mathbf{u} + \Phi \tag{5}$$

$$de = \left(\frac{\partial e}{\partial T}\right)_\rho dT + \left(\frac{\partial e}{\partial \rho}\right)_T d\rho = c_v dT + \frac{1}{\rho^2}\left(p - \frac{\alpha T}{\kappa}\right) d\rho \tag{6}$$

The change in internal energy is defined by the thermodynamic relation in Equation 6. For liquid hydrogen, the density variation term in Equation 6 has significant contribution, so this term needs to be included in the Equation 5 for accurate modeling. However, the geometrical reconstruction and backward projection of the VOF formulation are purely based on the assumption of conservation of liquid volume. In order to conserve total liquid mass, one must assume the liquid density to be constant. Thus, a physics-accurate internal energy formulation cannot be easily implemented alongside the VOF formulation.

The aforementioned problem is solved by representing the total energy conservation in a different thermodynamic state variable, enthalpy. Internal energy and enthalpy are related in Equation 7. Unlike the internal energy variation (Equation 6), the enthalpy variation (Equation 8) does not depend on density, and therefore this formulation is consistent with the VOF method. Substitution of Equation 7 in Equation 5 leads to the enthalpy-based total energy conservation

(Equation 9). Finally, Equation 8 is used to obtain the conservation equation for the primitive solved variable, i.e., temperature (Equation 3). Note that regardless of the representative form, the property being conserved is total energy, which for our purpose is summation of internal energy and kinetic energy.

$$e = h - \frac{p}{\rho} \tag{7}$$

$$dh = \left(\frac{\partial h}{\partial T}\right)_p dT + \left(\frac{\partial h}{\partial p}\right)_T dp = c_p dT + \frac{1}{\rho}(1 - \alpha T) dp \tag{8}$$

$$\rho \frac{Dh}{Dt} = \frac{Dp}{Dt} + \nabla(k \nabla T) + \Phi \tag{9}$$

C. Phase Change Mass Transfer

The mass transfer rate due to phase change between the gas and liquid phases ($\dot{m}$) is based on the model described by Hertz-Knudsen-Schrage (HKS) (Equation 10) [28], where all quantities are represented in SI units. HKS equation is based on statistical mechanics and thermodynamics states of the phases, and heat transfer is not considered. The HKS equation works well near-equilibrium condition. Note: The superscripts denote the variables that the root variable is the function of, i.e., $p_{sat}^{T_l}$ means the saturation pressure is function of liquid temperature. Temperature and pressures are continuous at the interface, i.e., $T_{sat} = T_l = T_g$.

Mathematically at saturation condition and at equilibrium, $C_{evap} = C_{cond}$ must be true. For self-pressurization problems, since the heat leakages are low compared to the internal energy of the system, gas is always near saturation condition, and since mass transfers would be very low, near-equilibrium condition is also always satisfied. With these assumptions, we write simplified HKS equation (Equation 11), which is from here referred to as HKS equation for brevity. Note that the accommodation factor ($0 < C_m \leq 1$) must be supplied, and its choice is discussed in *Effect of Accommodation Factor* section below.

$$\dot{m} = \sqrt{\frac{1}{2\pi R_g}} \left(C_{evap} \frac{p_{sat}^{T_l}}{\sqrt{T_l}} - C_{cond} \frac{p_g}{\sqrt{T_g}} \right) A_{in} \tag{10}$$

$$\dot{m} = C_m \sqrt{\frac{1}{2\pi R_g T_{in}}} \left(p_{sat} - p_g \right) A_{in} \tag{11}$$

Saturation pressure is obtained using Antoine equation (Equation 12), where the constants for a given fluid are sourced from NIST thermodynamic data set.

$$log_{10} p_{sat} = a - \frac{b}{c + T_{sat}} \tag{12}$$

D. VOF Transport

To consider the liquid phase, an additional equation for liquid volume fraction, F, to track the location of liquid phases is solved in CFDRC's VOF module. The volume fraction represents the local fraction of the cell volume occupied by the liquid of interest. All cells where the volume fraction is between 0.0 and 1.0 are interface cells in which both fluids and the interface between them exist. The spatial and temporal evaluations of the liquid volume fraction are given by the following Equation:

$$\frac{\partial F}{\partial t} + u_i \frac{\partial F}{\partial x_i} = 0 \tag{13}$$

The above Equation is nothing but a scalar transport equation. However, the advection of the above VOF field using conventional finite-volume discretization techniques is highly diffusive and leads to "smoothing" and destruction of the sharp interface between gas and liquid. To keep the sharp interface for a very long simulated periods, the initialization and transport are carried out using purely geometric constructions.

The simulation of two-phase flows with VOF methods consists of three main aspects:

1) VOF initialization, interface construction, and advection of liquid phase

2) Evaluation of body forces due to gravity and surface tension
3) Coupling of body forces and density changes to the solved pressure, momentum, and energy equations

The essential formulations of each of these aspects are provided in the following sections.

1. VOF Initialization

The VOF in each cell that contains the interface is given by the ratio of the liquid volume inside the cell to the cell volume (Equation 14). An example of a VOF initialization on a simple grid is shown in Figure 3. Interface cell properties are density averaged.

$$F_{cell} = \frac{V_l}{V_{cell}} \tag{14}$$

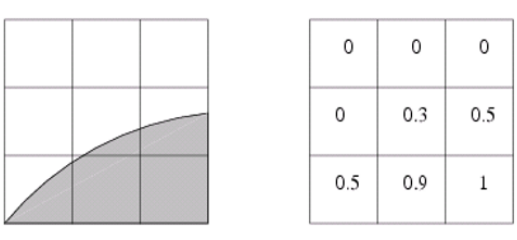

Fig. 3 True interface location (left) and corresponding volume fraction (right) in cells

2. Interface Reconstruction

In the VOF approach, the fluid interface needs to be "constructed" in each cell based on the knowledge of the VOF distribution in the neighboring cells [29]. Estimation of the interface location based on a known distribution of VOF on the grid has been tackled in multiple ways over the last few decades. Starting with a simple line interface calculation (SLIC) [30] method, the interface can be one or, in some cases, two lines aligned with the cell faces. In the SLIC approach the interface in each cell is linear i.e., a line ($a_1x + a_2y + C = 0$) in pure 2-D cells and a plane in ($a_1x + a_2y + a_3z + C = 0$) 3-D cells.

The gas-liquid interface in each cell then becomes a polygon (line-segment in 2-D) obtained by the intersection of the plane defining the interface and the cell faces. A schematic for such an interface is shown (in 2-D for a better understanding) in Figure 4. The SLIC method is, at best, a first-order reconstruction as the interface always returns a line. The piece-wise linear interface calculation (PLIC) method is obtained mainly from the approach of Parker and Youngs [31].

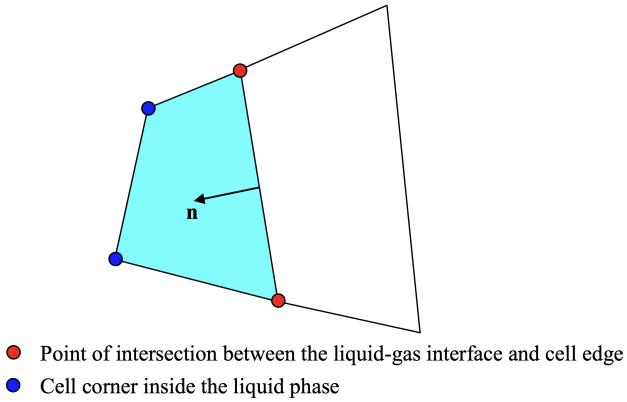

Fig. 4 2-D quad cell with interface between liquid phase (blue) and gas phase

Following Youngs' work, the interface in each cell is represented by a plane. The plane can be defined by Equation 15, where $\hat{n}$ is the unit normal to the plane and is also the normal to the VOF function F, $\mathbf{x}$ is any point on the plane, and C is a constant. Note the form of Equation 15 can be obtained from any generic plane equation ($a_1x + a_2y + a_3z + C = 0$) by normalizing a_i to corresponding components of the unit normal vector.

$$\hat{\mathbf{n}} \cdot \mathbf{x} + C = 0 \tag{15}$$

For constructing an interface in the cell, two main quantities are required:

1) An estimate of the interface normal $\hat{n}$
2) The value of the VOF (F_{cell})

F_{cell} is known at initialization. It is also known at every advection time step. The interface normal is generally obtained by using the gradient of the VOF function F_{cell} as in Equation 16.

$$\hat{\mathbf{n}} = \frac{\nabla \mathbf{F}}{|F|} \tag{16}$$

This normal points towards the liquid phase as required for the interface reconstruction algorithm discussed later. The accuracy of the unit normal evaluated by Equation 16 is dictated by the accuracy of the gradient evaluation technique. This unit normal also determines the orientation and the area of the interface. Significant physical quantities - the surface-tension source terms and phase change mass transfer - depend on the accuracy of evaluation of the surface normal in each cell that contains the interface.

Once the unit normal to the interface is known in a cell, the constant C in Equation 15 is evaluated using very specific techniques [29]. The problem consists of determining the constant C of the plane P (Equation 15) with a given normal $\hat{\mathbf{n}}$, which truncates the cell polyhedron Ω producing a polyhedron Ω_T whose volume matches the volume of liquid in the cell. The actual method involves bracketing the solution for C using the vertices of the original cell polyhedron. This is followed by a process similar to the bisection algorithm until the cut polyhedron volume matches the liquid volume. The implementation provided by [29] is used with the VOF module to create the liquid polyhedron in all the cells containing the gas-liquid interfaces.

3. Interface Advection

The amount of liquid volume fraction advected through a cell face is computed by the backward projection of the upwind cell face. At every cell face, we first calculate $\mathbf{u}_{\mathbf{face}} \cdot \hat{\mathbf{n}}_{\mathbf{face}}$. Each face of the cell is then projected backward, as shown in Figure 5, into the upwind direction, i.e., into the leftward cell to the face if $\mathbf{u}_{\mathbf{face}} \cdot \hat{\mathbf{n}}_{\mathbf{face}} > 0$ and into the rightward cell to the face if $\mathbf{u}_{\mathbf{face}} \cdot \hat{\mathbf{n}}_{\mathbf{face}} < 0$. The left and right cells with respect to a given face are indicated by the direction of the face normal vector, i.e., the face normal vector points from the left cell into the right cell. The face is then projected backward by a distance $(\mathbf{u}_{\mathbf{face}} \cdot \hat{\mathbf{n}}_{\mathbf{face}})\Delta t$, where the time step Δt is set to satisfy a maximum Courant-Fredericks-Lewy (CFL) criterion.

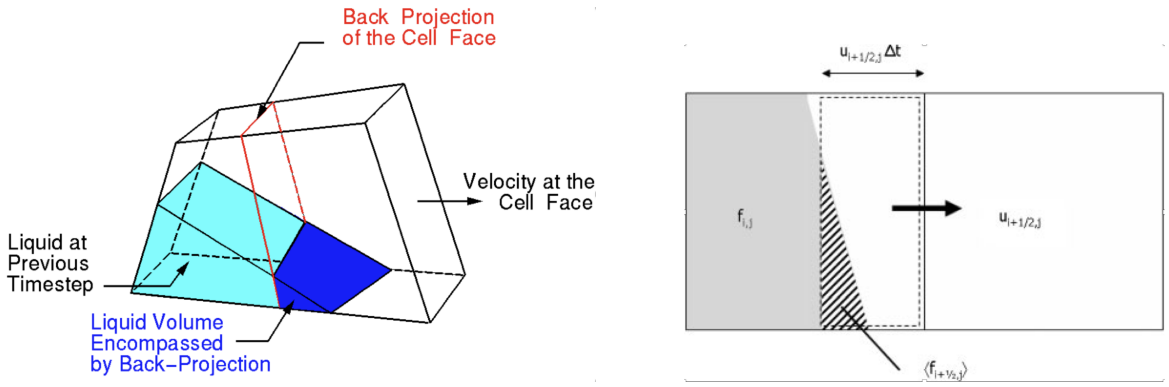

(a) 3D Rendering **(b) 2-D Rendering**

Fig. 5 Illustrations of VOF Advection using Back-Projection

The convex liquid polyhedron in the upwind (or donor) cells is truncated by the plane containing the back-projected face. The volume of the cut liquid polyhedron is added to the face flux from the upwind to the downwind cell. The net change in VOF in each cell then becomes the net summation of liquid volume fluxes in and out of the cell. As a result, the Equation solved during VOF advection (Equation 17) is the integrated version of Equation 13 on a control volume, V and control surface, S.

$$\frac{\partial}{\partial t}\iiint_V \rho F \, dV + \iint_S \rho \mathbf{u} \cdot \hat{\mathbf{n}} F \, dS = 0 \tag{17}$$

The implementation requires the development and use of algorithms to intersect convex liquid polyhedrons with planes defined by the back-projected cell face [29].

4. Surface Tension

The forces due to liquid surface tension are estimated using work similar to that done by Yang et al. [32]. Yang et al discovered several deficiencies in the continuum surface force (CSF) model of Kothe and Rider [20]. These include convergence difficulties in capillary flows, problems due to a non-smooth unit normal vector, and problems recovering correct physics when the grid size is reduced. To remedy this, a conservative formulation for the calculation of surface tension force was implemented. The formulation is based on equilibrium of a curved surface under surface tension as shown in Figure 6.

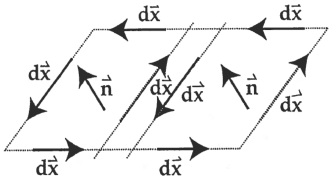

Fig. 6 Equilibrium of a Free Surface under Surface Tension

The net normal force acting on the surface is equal to the summation of all the tangential forces due to surface tension. Thus, the pressure rise across an interface can be deduced as in Equation 18.

$$\iint_{surface} \Delta p \, \mathbf{dS} = \int_{boundary} \sigma \hat{\mathbf{n}} x \, dx \tag{18}$$

Here the integral along the common edge of adjacent interfaces cancels out due to the opposite traversal of the line integrals. The liquid-gas interface for surface tension force calculation is assumed to be at the $F = 0.5$ location deduced from the nodal values of F. The unit normal for Equation 6 is obtained based on Equation 16. This approach has been implemented within the VOF module for evaluating the surface tension forces. This formulation was seen to work very well with validation problems, including droplets under surface tension. The surface tension force normal to the interface is applied as a source term in the momentum equation and acts only in the interfacial cells.

E. Coupling between VOF Module and Flow Solver

For two-phase flow with gas-liquid interfaces, the density is not constant in space, and therefore the full continuity equation must be solved (Equation 19).

$$\frac{\partial \rho}{\partial t} + \nabla \cdot (\rho u) = \frac{\partial \rho}{\partial t} + \iint_{surface} (\rho_f u_f) \cdot n_f \tag{19}$$

In order to maintain consistency between the VOF module and Loci-Stream flow solver, appropriate face density values are required. The face densities cannot be modeled as the current Stream implementation uses inverse distance weighted values from the cell centers. Instead, a new implementation of the face densities was carried out as in Equation 20.

$$\rho_f = \frac{\rho_g \dot{V}_g + \rho_l \dot{V}_l}{\dot{V}_g + \dot{V}_l} \tag{20}$$

where, $\dot{V}_g$ and $\dot{V}_l$ denote the gas-volume and liquid-volume fluxes across the face at a given time step. This approach is expected to provide a consistent formulation between the explicit VOF advection and the implicit Stream time-step advances.

Stream utilizes the cell densities based on advected VOF and the new face densities. This provides it with the information of how much mass is to be "fluxed" into each cell to solve the pressure correction and then the momentum equations.

Based on the previous work by Lowry and Yang [33], the formulation for the pressure correction equation was modified so that it uses $ln(\rho)$ for the source term of the p' equation as recommended by Pericleous et al. [34] using a total derivative form of $ln(\rho)$ to represent mass conversation (Equation 21).

$$\frac{D(ln\,\rho)}{Dt} + \nabla u = 0 \tag{21}$$

F. Lumped Gas CFD Model

Since the wall heat fluxes are low in the self-pressurization problems, the ullage is always near equilibrium condition, i.e., the ullage pressure and gas-liquid interface saturation pressure are similar and do not deviate far from each other. With that assumption, the self-pressurization problem can be simplified by recognizing that (i) the gas-liquid interface is quiescent and does not move throughout the experiment because the phase change rate is very small; (ii) the gas phase holds a very small (about two orders of magnitude smaller) fraction of internal energy than the liquid propellant; and (iii) liquid side interfacial thermal stratification dominates the dynamics of the problem. With these observations, we can disjoint the liquid and gas phase CFD and do away with employing the computationally expensive VOF module. Instead, we model the gas phase as a lumped node and communicate fluid-thermal information from the ullage as a uniform boundary condition to the time-accurate liquid CFD (Figure 7). A similar approach has been promulgated by Barsi and Kassemi [35], with somewhat different implementation treatment. This type of approach provides two advantages. First, the simulation is much more computationally efficient because it avoids the geometric reconstruction and advection steps of the VOF method. Second, the allowable time step size is an order of magnitude larger than with VOF, which has stringent maximum Courant number restrictions for stability. This effect is exacerbated by mesh refinement and very small spurious velocities at the interface that can force the time step to drop further. The lumped gas model alleviates this requirement and higher mesh resolutions can be easily used to capture the thermal gradient layer near the interface.

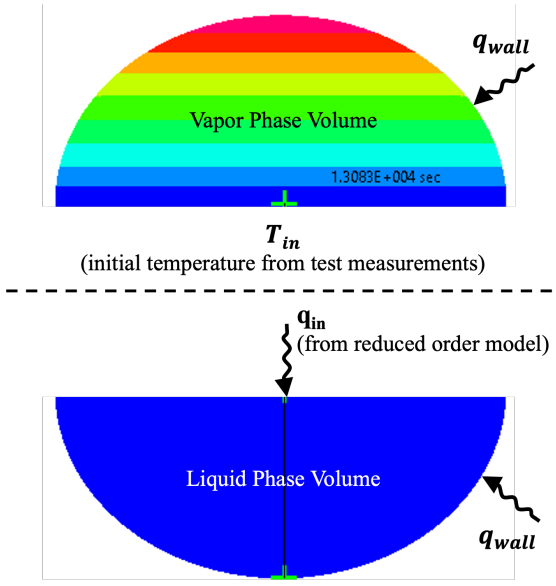

Fig. 7 Schematic of lumped gas liquid CFD model

The interfacial heat balance (Equation 22) thermally couples the liquid and gas in this model. The gas thermal diffusion term is related to Equation 22 by internal energy balance in the ullage via Equation 23. Combining these two

equations yields Equation 24, which describes the liquid interface boundary condition, where the time rate of change of ullage temperature and phase change mass transfer is obtained by the lumped ullage gas model.

$$\iint_{in} k_g \nabla T_g \, dA_{in} = \iint_{l} k_l \nabla T_l \, dA_{in} + \dot{m} L \tag{22}$$

$$\iiint_{V_g} \rho_g c_{vg} \frac{\partial T_g}{\partial t} \, dV_g = - \iint_{in} k_g \nabla T_g \, dA_{in} + \iint_{g_{wall}} \dot{q}_{g_{wall}} \, dA_{g_{wall}} \tag{23}$$

$$\iint_{in} k_l \nabla T_l \, dA_{in} = \dot{Q}_{g_{wall}} - m_g c_{vg} \frac{\partial T_g}{\partial t} - \dot{m} L \tag{24}$$

For the lumped gas model, first we mathematically decompose the ullage temperature by summation of two parts: liquid interface temperature, T_i, and the difference between the ullage and liquid interface temperature (ΔT). The former is obtained from the liquid side of the interface and is therefore only a function of time and spatial coordinates in the liquid domain, i.e., independent of ullage spatial coordinates. The latter is a function of both time and coordinates in the ullage domain (Equation 25). Note again that the superscripts denote the variables that the root variable is the function of, i.e., $T_g^{t,x_{gi}}$ means the gas temperature is function of time and ullage spatial coordinates.

$$T_g^t = T_{in}^{t,\mathbf{x_l}} + \Delta T_g^{t,\mathbf{x_g}} \tag{25}$$

The reduced order model (ROM) for the ullage seeks to best estimate the $\Delta T_g^{t,\mathbf{x_g}}$ term as function of time only - independent of ullage spatial coordinates, so that the gas can be represented as a node in the CFD simulation of the liquid. We achieve this by conducting an ullage-only CFD analysis. A fixed temperature no-slip wall boundary condition at the gas-liquid interface is imposed, so the ullage CFD is fully decoupled from the liquid side. Later, when running liquid CFD, coupling is achieved by calculating gas temperature as described in Equation 25. This approximation is valid due to the reasons discussed above. In the *Results* section, the accuracy of the approach is demonstrated.

The ullage temperature difference term ($\Delta T_g^{t,\mathbf{x_g}}$ may be deduced in two ways with varying complexity. In the simpler approach, a steady state ullage CFD solution provides this term independent of time (Equation 26). In the second approach, unsteady ullage CFD is used to obtain a time-accurate representation of the temperature difference (Equation 27. In fact, our testing showed that the time-dependent and time-independent solutions only differ slightly in capturing the initial pressurization transient and are equally good at prediction of long-term pressurization rates. The primary difference lies in time-accurate prediction of ullage temperature only. Both approaches are very economic when compared to the VOF module.

$$T_g^t = T_{in}^{t,\mathbf{x_l}} + \frac{\iiint_{V_g} T_g^{t=\infty} \, dV_g}{\iiint_{V_g} dV_g} \tag{26}$$

$$T_g^t = T_{in}^{t,\mathbf{x_l}} + \frac{\iiint_{V_g} T_g^t \, dV_g}{\iiint_{V_g} dV_g} \tag{27}$$

The phase change mass transfer in Equation 24 is obtained by considering that the ullage is always near saturation condition. The Antoine relation (Equation 12) is used to calculate gas pressure (Equation 28) as a function of gas-liquid interface temperature T_{in}. Subsequently, ullage mass and rate of change of mass are calculated as per Equation 29 and 30. Incorporating, Equation 27 and 30 in 24 closes the liquid CFD boundary condition. Results are compared with the experiment and the VOF module approach in the *Results* section.

$$P_g^t = P_{sat}^{T_{in}^t} = 10^{\left(a - \frac{b}{c + T_{in}}\right)} \tag{28}$$

$$m_g^t = \frac{P_{sat}^t V_g}{R_g T_g^t} \tag{29}$$

$$\dot{m}^t = \frac{m_g^t - m_g^{(t-dt)}}{\Delta t} \tag{30}$$

V. Validation of K-site Problem

A. Geometry

The full 3-D geometrical model of the K-site experiment tank is shown in Figure 8. As axisymmetric flow with respect to the tank axis is expected, a 11.25° sector model is used to save simulation time. Tank internals are not considered as they insignificant for the problem dynamics but removing them simplifies the mesh and makes CFD simulation more robust.

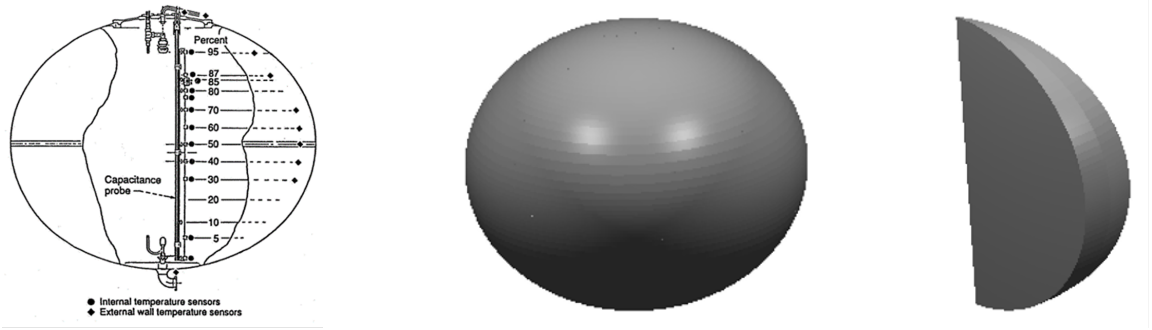

(a) Tank schematic **(b) Simplified domain** **(c)** 11.25 deg **sector**

Fig. 8 K-site LH2 tank and simplified sector for CFD simulation

B. Mesh

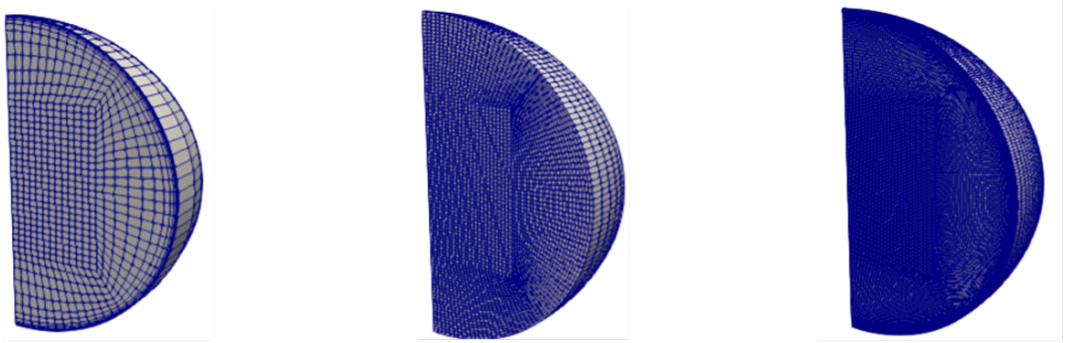

(a) Coarse **(b) Baseline** **(c) Refined**

Fig. 9 Mesh resolutions used for validation and verification

The initial mesh for the sector is shown in Figure 9a. This mesh has a resolution equivalent to 4 million cells for the full 3-D model, a typical size used for propellant slosh applications. The experimental pressurization time is around 20 h. A variable stable time step size is picked by the VOF module based on a set maximum CFL number. To complete one simulation with the VOF module for the baseline mesh (Figure 9b), approximately one month of clock time is required on NASA's advanced super-computing system (NAS). As shown in Figure 9, three different mesh resolutions were tested. Later it is shown that the refined mesh (Figure 9c) is necessary for accurate fluid and thermal dynamics resolution.

C. Initial and Boundary Conditions

Both gas and liquid are at saturation conditions at the beginning of the simulation ($T = 20.35\,\mathrm{K}$ and $p = 1.036 \times 10^5\,\mathrm{N/m^2}$). On the tank wall, the no-slip condition is applied for the momentum equation, and a uniformly distributed constant heat flux is used for the energy equation. Two heat flux values from the experiment, $2.0\,\mathrm{W/m^2}$ and $3.5\,\mathrm{W/m^2}$, are simulated for each of the 29% and 49% fill level cases. On the sector planes, a symmetry condition is applied.

D. Fluid Properties

Fluid and material properties were evaluated from the current National Institute of Standards and Technology (NIST) databases [36]. The liquid properties are listed in Table 1. The gas is assumed to be an ideal gas and the properties are taken from the existing thermodynamic table in Loci-Stream and NIST [36].

Parameters	Description	Value
ρ_l	Liquid density	$70.734\,\mathrm{kg/m^3}$
c_{vl}	Liquid specific heat at constant volume	$5678.2\,\mathrm{J/Kg/K}$
c_{pl}	Liquid specific heat at constant pressure	$9516.0\,\mathrm{J/Kg/K}$
k_l	Liquid thermal conductivity	$0.1034\,\mathrm{W/m/K}$
μ_l	Liquid dynamic viscosity	$1.324 \times 10^{-5}\,\mathrm{kg/m/s}$
α_l	Liquid volume expansion coefficient	$0.0168\,\mathrm{K}$
κ	Liquid iso-thermal compressibility	$1.8662 \times 10^{-8}\,\mathrm{K}$
L	Latent heat	$4.451 \times 10^{5}\,\mathrm{J/kg}$
σ	Surface tension	$0.002\,005\,1\,\mathrm{N/m}$

Table 1 Liquid Hydrogen Thermodynamic Properties

E. Flow Regime and Simulation Options

Both laminar and turbulent flow regimes are evaluated. Two turbulence models are considered: the RANS k-ω shear stress transport model (k-ω-SST), and the k-ω SST Delayed Detached Eddy Simulation (DDES), which is a hybrid RANS-LES model. Time integration is computed implicitly with first-order backward Euler method. Time step size for the gas phase was set to $dt = 1 \times 10^{-2}$ s for all cases. The VOF module is able to reduce the time step for stability requirements as necessary. For this purpose, a maximum CFL number of 0.2 was chosen. Based on experience with slosh dynamics with the VOF module, a first-order accurate spatial stencil was employed.

The Antoine equation is used for the calculation of the saturation condition. The accommodation factor coefficient in the phase change model is set to 1.0×10^{-3}. The sensitivity of this parameter is reported in *Effect of Accommodation Factor* section.

VI. Results

As the changes in mass and energy during self-pressurization are relatively small compared to typical CFD applications, iterative solution convergence for all governing equations was closely monitored. Further, for this large time scale simulation, total mass and energy conservation were also verified explicitly to ensure there was no significant accumulation of error. Since the total energy conservation is enforced using temperature as a primary solved variable, special care has been taken to maintain total energy conservation. Solution verification via mesh refinement was also performed to achieve a mesh independent solution and is presented in a subsequent section. Further, sensitivity to the flow regime (laminar vs. turbulent) and accommodation factor (AF) is evaluated.

First, simulations of the K-site self-pressurization experiments at multiple fill levels and heat loads were conducted using a relatively coarse mesh. The coarse mesh enables a simulation of a rather long pressurization duration (20 hours) to be finished in a reasonable time (typically a few days) to allow for a quicker evaluation.

Typical velocity and temperature fields are shown in Figure 10. Due to the buoyancy effect, a large recirculation is formed in the liquid phase, and the warmer and lighter liquid from the tank wall boundary is carried upwards towards the gas-liquid interface, where it evaporates if the interfacial temperature is higher than the saturation pressure set by the gas phase. The typical thermal boundary layer and temperature stratification in the gas phase is also observed. These observations provide qualitative validation that, even with a coarse mesh, the CFD model is capturing the proper physics.

For quantitative validation, pressure history comparisons between the experiment and CFD predictions (using the finest resolution mesh (Figure 9c)) at both $2.0\,\mathrm{W/m^2}$ and $3.5\,\mathrm{W/m^2}$ heat load, and both 29% and 49% fill conditions, are presented in Figure 11 (i), (ii), (iii), and (iv). Both VOF CFD and lumped gas CFD models show good agreement with the experimental data, and clearly demonstrate the ability of the tools to accurately predict self-pressurization. Initially,

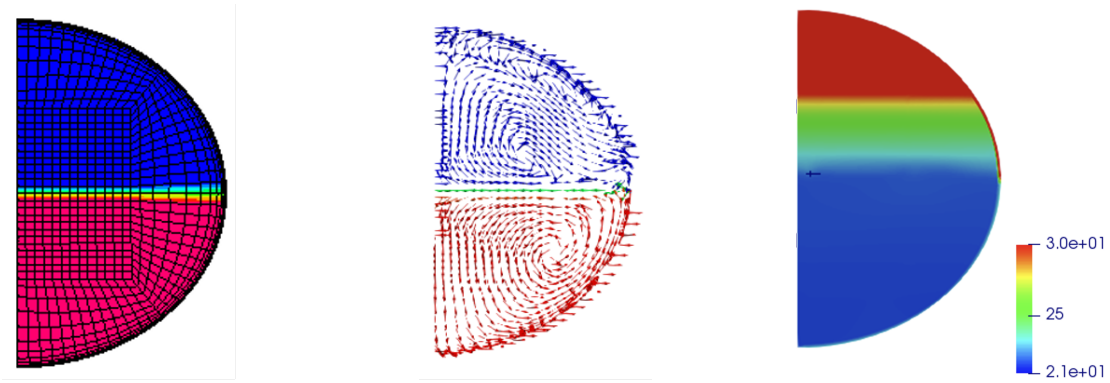

(a) Initial Liquid-Gas Distribution **(b) Velocity Field** **(c) Temperature Field**

Fig. 10 K-site VOF, Velocity and Temperature Field with Coarse Mesh for $3.5\,\mathrm{W/m^2}$ Heat Load

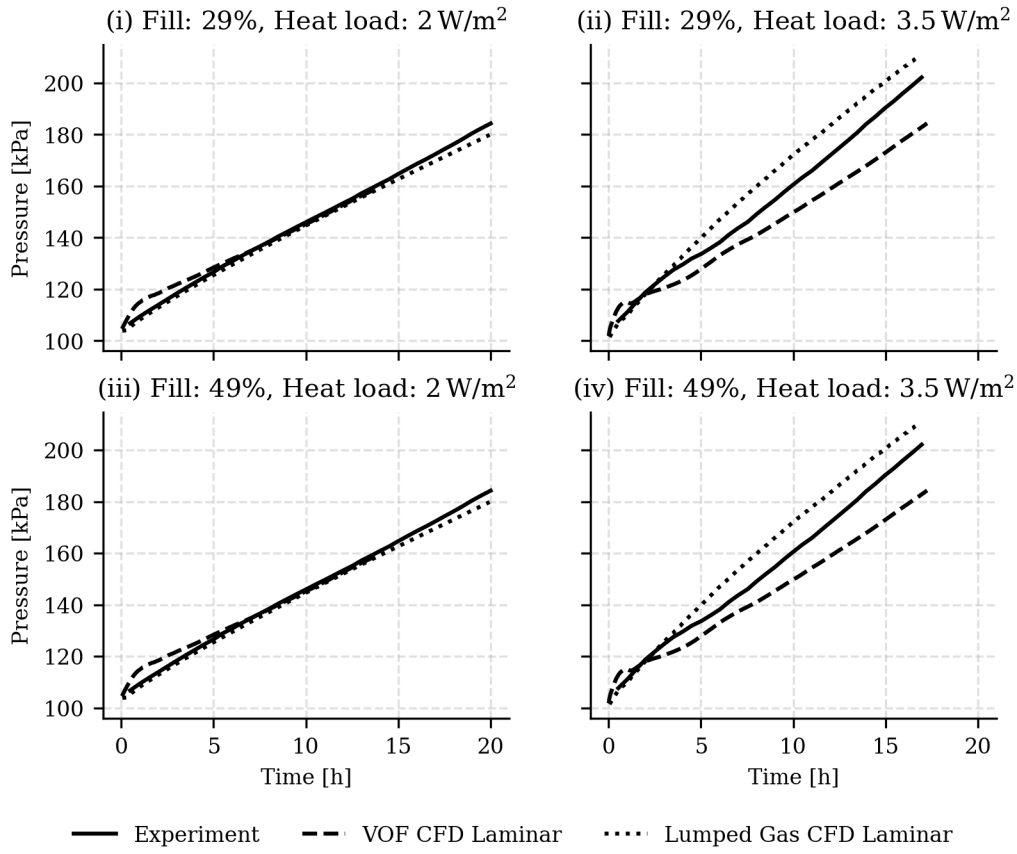

Fig. 11 Comparison of pressurization for K-site LH2 tank at 29% and 49% fill with $2.0\,\mathrm{W/m^2}$ and $3.5\,\mathrm{W/m^2}$ heat load

the evaporation rate is higher as warm buoyancy-driven liquid advects to the gas-liquid interface and evaporative mass transfer takes place. Later, the increasing ullage pressure dampens the evaporation rate and a quasi-steady state with constant pressurization rate is achieved. The VOF CFD shows a slight overshoot in pressure in the initial transient, which may be due to small interfacial instabilities encountered in the VOF module. But the overall trend is captured well by both CFD models.

Temperature probes were also compared, showing excellent time-accurate agreement with the K-site experiments

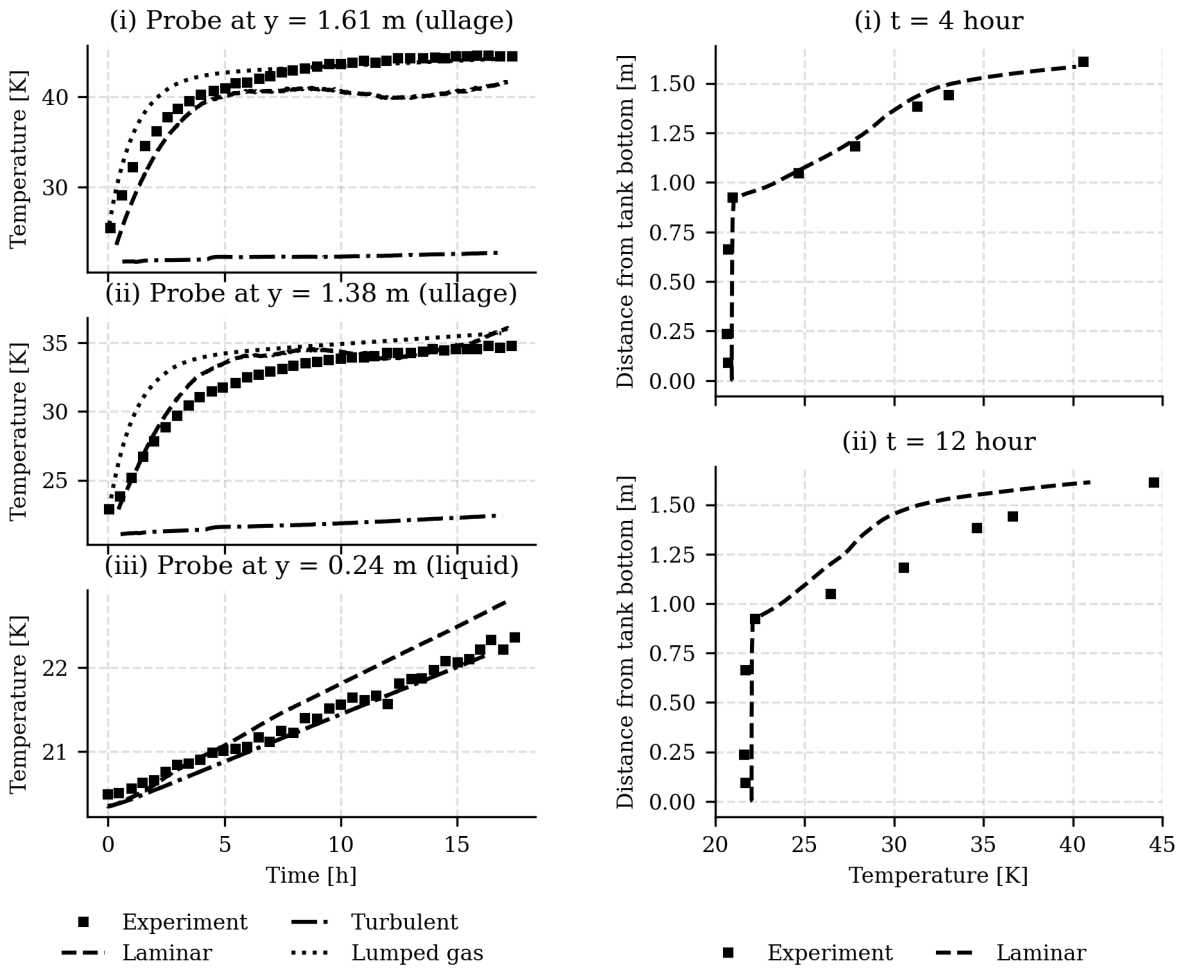

(a) Probe temperatures at 1.61 m, 1.38 m, and 0.24 m

(b) All temperature probes at 4 h and 12 h

Fig. 12 Probe temperatures for K-site LH2 tank at 49% **fill with** $3.5\,\mathrm{W/m^2}$ **heat load**

for both ullage (Figure 12a (i) and (ii)) and liquid (Figure 12a (iii)). Figure 12b shows a comparison of all probes at (i) 4 hours, and (ii) 12 hours elapsed time. The agreement with experimental data for both VOF and lumped gas models emphasizes how well the flow field is resolved and energy conservation is maintained, both of which must be simultaneously achieved for an accurate solution. Note that the turbulent flow model fails at capturing the temperature trends in the ullage (Figure 12a (i) and (ii)), which is be discussed in the *Flow Regime Sensitivity* section below.

A. Verification: Sensitivity to Mesh Resolution

Mesh independence was ensured by simulating three different mesh resolutions. It is observed that while the coarsest mesh (Figure 13(i)) produces good qualitative predictions, the pressurization rate is under-predicted when compared to the experimental data. Further mesh refinement to the baseline mesh improves the prediction by better capturing the convective currents and thermal stratification in the liquid phase. Finally, the finest mesh produces the best match with the experiment by further improving the accuracy of the interfacial liquid thermal layer resolution. Note that further mesh refinement may produce slight improvements in the predicted pressurization rate, though the prohibitively high cost of such CFD simulations is not justified by small improvements in predictive capability.

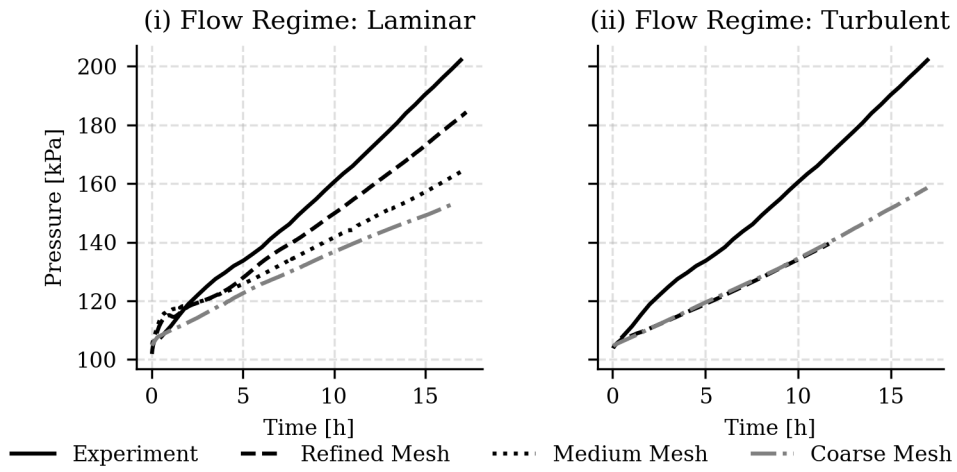

Fig. 13 Mesh sensitivity for K-site LH2 tank at 49% fill with $3.5\,\mathrm{W/m^2}$ heat load with VOF CFD

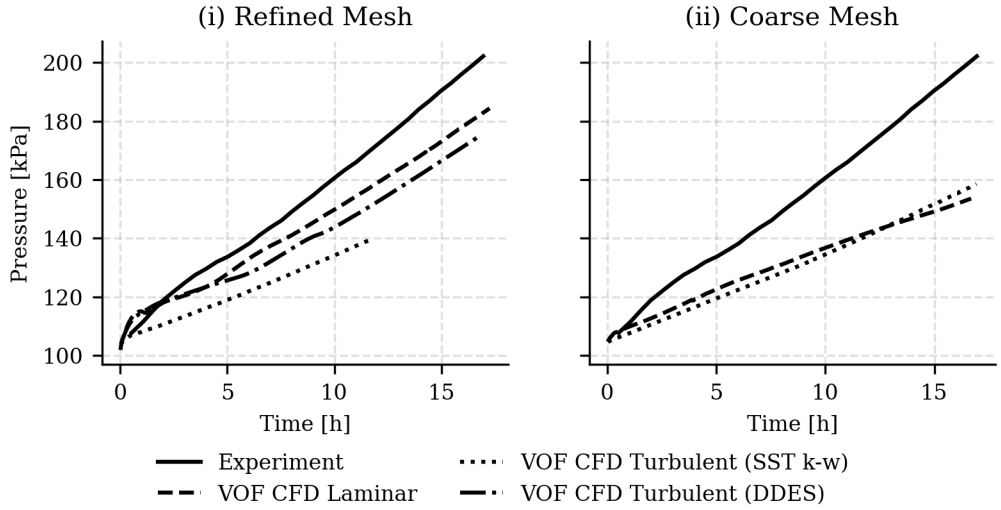

Fig. 14 Flow regime sensitivity for K-site LH2 tank at 49% fill with $3.5\,\mathrm{W/m^2}$ heat load with coarse and refined mesh resolution

B. Flow Regime Sensitivity

Models for both laminar and turbulent flow regimes were tested and compared with the experimental results (Figure 14). The $k-\omega$ SST RANS model under-pressurizes. This is due to high turbulent viscosity in the interfacial region. The resulting high momentum and thermal diffusivity smears out the liquid side thermal stratification, which plays a very important role in the dynamics of the problem. Note that bulk liquid away from the interface is not adversely affected (12a (iii)). But capturing the liquid side interfacial temperature is extremely important because it dictates the computation of the saturation pressure and the mass transfer rate in the phase change model and thus dictates the pressurization rate. The observation of high momentum and thermal diffusivity produced by the RANS model is further reinforce by examining the effect of mesh resolution on the turbulent flow simulations (Figure 13(ii)). Coarse meshes are numerically diffusive and artificially increases the viscosity, but mesh refinement reduces this effect. Figure 13 shows no change in pressurization rate with the refined mesh - in contrast with the laminar flow regime behavior - demonstrating the high diffusivity generated by the turbulence model.

The root cause of the $k-\omega$ SST model's failure to capture the thermal stratification in the gas-liquid interface region seems to lie in the origin of the turbulence modeling. The model was developed for single phase applications

and employing the same model simultaneously for liquid and gas species with a continuous turbulent kinetic energy and turbulent dissipation field, which is unlikely to be accurate description of the underlying physics encountered at a gas-liquid interface. A more sophisticated RANS turbulence model is necessary for two phase VOF class of applications. The $k-\omega$ DDES (hybrid RANS-LES) model implemented in Loci-Stream slightly improves the prediction of the SST model because it is less diffusive than the RANS model but is still inferior to the laminar model in predictive capacity. More studies are underway to improve the understanding of turbulence modeling, meanwhile laminar modeling is recommended for this class of problem.

C. Effect of Accommodation Factor

Since the HKS model (Equation 11) for phase change mass transfer has an accommodation factor (AF) that drives the evaporation/condensation rates but does not have an empirically-derived value, it is necessary to demonstrate the impact of AF on the validation. Higher AF results in higher mass transfer rate in the model, but it does not necessarily linearly impact the observed phase change rate because higher mass transfer rate also increases the ullage pressure in a closed system, which in turn lowers the mass transfer rate. Moreover, the self-pressurization process is driven by a small heat leakage in a closed system where the interface is always near equilibrium. In this case, the pressurization rate is expected to be insensitive to AF in a reasonably large range and converge logarithmically as the value approaches unity.

For choosing an AF value, the available literature suggests that AF is dependent upon substance and operating conditions, though experimentally tested values are difficult to characterize and obtain. Our literature review did not find a definitive AF value for hydrogen at the given operating condition. Previously, for a different simulation, we had found that 1×10^{-5} is too low to produce sufficient pressurization. Therefore, we assessed the model sensitivity for the K-site simulations by using AF values of 1×10^{-4}, 1×10^{-3} and 1×10^{-2}. We found that the AF of 1×10^{-2} and higher was difficult to simulate due to extremely low time-step required for numerical stability. Figure 15 shows that the AF of 1×10^{-4} has a reasonably insignificant impact on the K-site pressurization rate. Although there is a small difference in the transient behavior in the early part of the simulations, there is little difference between the near-constant pressurization rates predicted when the simulation has reached a quasi-steady state. These observations indicate that an AF above a minimum threshold (approximately 1×10^{-4}) does not yield any significant change in self-pressurization rates for a closed quiescent system.

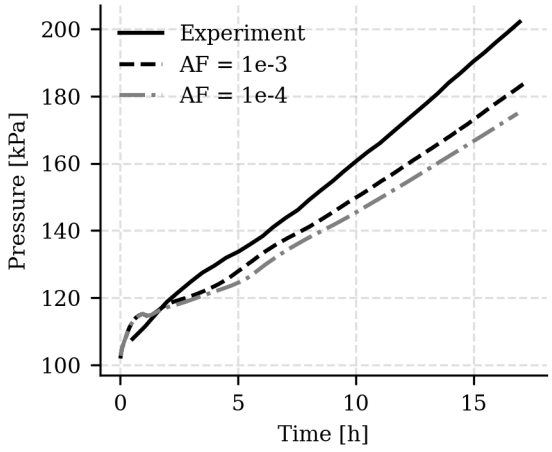

Fig. 15 Accommodation factor sensitivity for K-site LH2 tank at 49% fill with $3.5\,\mathrm{W/m^2}$ heat load

VII. Conclusion

The Loci-Stream CFD tool has been shown to be validated against the K-site LH2 tank self-pressurization experiments. For four different test configurations, both the VOF method and the lumped gas ROM method demonstrate accurate predictive capability. Loci-Stream is able to predict both time varying ullage pressure as well as liquid and gas temperatures at various spatial locations for all simulated experiments with acceptable accuracy. While the Loci-Stream-VOF model is capable of simulating the heat and mass transfer physics of self-pressurization, the

computational expense required to resolve the important thermal gradients near the interface over such large time scales may be too prohibitive to be useful to support a flight project schedule. It was demonstrated that the reduced order model provides an order of magnitude (or more) speed up without degradation of the solution, and a more general segregated gas/liquid domain approach is being pursued to augment the capabilities of Loci-Stream-VOF. We conclude that Loci-Stream-VOF and the reduced order lumped gas model are both well-equipped to simulate fluid and thermal dynamics of cryogenic tank self-pressurization to support NASA's future missions, and future work will assess and validate these tools for in-space (microgravity) conditions.

Acknowledgments

The NASA High-End Computing (HEC) Program, through the NASA Advanced Supercomputing (NAS) Division at Ames Research Center, provided the computational resources for these simulations.

References

[1] Huntley, S. C., "Temperature-pressure-time relationships in a cryogenic container," *Adv Cryog Eng*, Vol. 3, 1960, pp. 342–352.

[2] Neff, R., "A survey of stratification in a cryogenic liquid," *Adv Cryog Eng*, Vol. 5, 1960, pp. 460–466.

[3] Scott, L. E., Robbins, R. F., Mann, D. B., and Birmingham, B. W., "Temperature stratification in a nonventing liquid helium dewar," *J Res Nat. Bur. Stand. (U.S.), 64C (Eng. and Inst.)*, 1960.

[4] Swim, R. T., "The temperature distribution in liquid and vapor phases of helium in cylindrical dewars," *Adv Cryog Eng*, Vol. 5, 1960, pp. 498–504.

[5] Barsi, S., and Kassemi, M., "Investigation of tank pressurization and pressure control part ii: numerical modelling," *ASME J Therm Sci Eng Appl*, Vol. 5, No. 2 [041006], 2013, pp. 1–9.

[6] Barsi, S., and M., K., "Numerical and experimental comparisons of the self-pressurization behavior of an LH2 tank in normal gravity," *Cryogenics*, Vol. 48, No. 3-4, 2008, pp. 122–129.

[7] Grayson, G., Lopez, A., Chandler, F., Hastings, L., and Tucker, S., "Cryogenic tank modeling for the Saturn AS-203 experiment," *AIAA 2006–5258*, 2006.

[8] Panzarella, C. H., and Kassemi, M., "On the validity of purely thermodynamic description of two-phase cryogenic storage tank," *J Fluid Mech*, Vol. 484, 2003, pp. 136–48.

[9] Kassemi, M., and Chato, D., "The zero boil-off tank experiment, Cold Facts," *Cryogenic Society of America*, Vol. 33, 2017, p. 3.

[10] Kartuzova, O., and Kassemi, M., "Modeling ullage dynamics of tank pressure control experiment during jet mixing in microgravity," *AIAA 52nd joint propulsion conference. Salt Lake City, UT*, 2016.

[11] Kassemi, M., and Olga, K., "Effect of interfacial turbulence and accommodation coefficient on CFD predictions of pressurization and pressure control in cryogenic storage tank," *J Cryogenics*, Vol. 74, 2016, pp. 138–53.

[12] Doherty, M., Gaby, J., Salerno, L., and Sutherlin, S., "Cryogenic Fluid Management Technology for Moon and Mars Missions," *AIAA 2009-6532*, 2009.

[13] Kassemi, M., Kartuzova, O., and Hylton, S., "Validation of two-phase CFD models for propellant tank self-pressurization: Crossing fluid types, scales, and gravity levels," *Cryogenics*, Vol. 89, No. 2018, 2018, pp. 1–15.

[14] Moran, M. E., "Cryogenic Fluid Storage Technology Development: Recent and Planned Efforts at NASA," *NASA TM 2009-215514*, 2009.

[15] Ferrín, J. L., and Pérez-Pérez, L. J., "Numerical simulation of natural convection and boil-off in a small size pressurized LNG storage tank," *Comput. Chem. Res.*, Vol. 138, 2020, p. 10684.

[16] Unverdi, S. O., and Tryggvason, G., "A front-tracking method for viscous, incompressible, multi-fluid flows," *Journal of computational physics;*, Vol. 100, No. 1, 1992, pp. 25–37.

[17] Sussman, M., Fatemi, E., Smereka, P., and Osher, S., "An improved level set method for incompressible two-phase flows," *Computers & Fluids*, Vol. 27, No. 5, 1998, pp. 663–80.

[18] Osher, S., and Fedkiw, R. P., "Level set methods: an overview and some recent results," *Journal of Computational physics;*, Vol. 169, No. 2, 2001, pp. 463–502.

[19] Benson, D. J., "Volume of fluid interface reconstruction methods for multi-material problems," *Applied Mechanics Reviews*, Vol. 55, No. 2, 2002, pp. 151–65.

[20] Rider, W. J., and Kothe, D. B., "Reconstructing volume tracking," *Journal of computational physics*, Vol. 141, No. 2, 1998, pp. 112–52.

[21] Hasan, M., Lin, C., and Van Dresar, N. T., "Self-pressurization of a flightweight liquid hydrogen storage tank subjected to low heat flux," *NASA TM 103804*, 1991.

[22] Van Dresar, N. T., Lin, C., and Hasan, M., "Self-pressurization of a flightweight liquid hydrogen tank: Effects of fill level at low wall heat flux," *NASA TM 105411*, 1992.

[23] West, J., Yang, H. Q., and Liever, P. A., *Development, Verification, and Validation of Parallel, Scalable Volume of Fluid CFD program for Propulsion Applications*, JANNAF Conference paper, 2014.

[24] Luke, E., and George, T., "Loci: A Rule-Based Framework for Parallel Multidisciplinary Simulation Synthesis," , 2005.

[25] Thakur, S., Wright, J., and Shyy, J. W., "An Algorithm for Chemically Reacting Flows on Generalized Grids Using a Rule-Based Framework," *43rd AIAA Conference*, 2005, p. 0875.

[26] Kamakoti, R., Thakur, S., Wright, J., and Shyy, W., "Validation of a new parallel all-speed CFD code in a rule-based framework for multidisciplinary applications," *36th AIAA Fluid Dynamics Conference and Exhibit, AIAA 2006–3063, San Francisco, CA*, 2006.

[27] Mehta, R. S., Venugopalan, V., H. Q. Yang, J. W., and Thakur, S., *Development of a Highly Scalable Volume of Fluid Solver for Arbitrary Polyhedral Grids*, JANNAF Conference paper, 2015.

[28] Schrage, R. W., Columbia University Press, 1953, p. 27.

[29] Hernández, J. L., "Analytical and geometrical tools for 3D volume of fluid methods in general grids," *Journal of Computational Physics*, Vol. 227, 2008, pp. 5939–48.

[30] Hirt, C., and Nichols, B. D., "Volume of Fluid (VOF Method) For Dynamics of Free Boundaries," *Journal of computational physics*, Vol. 39, 1981, pp. 201–225.

[31] Parker, B., and Youngs, D. T. a., *and three-dimensional Eulerian simulation of fluid flow with material interfaces*, UK Atomic Weapons Establishment, 1992.

[32] Yang, H. Q., and Przekwas, A. J., "Computational Modeling of Microfluid Devices with Free Surface Liquid Handling," *Proceedings of the 1998 International Conference on Modeling and Simulation of Microsystems*, 1998, pp. 498–505.

[33] Lowry, S., and Yang, H. Q., *Numerical Model of the Fluid-Structure Interaction in the Space Shuttle External LOX Tank for Modified Baffle Configurations*, CFD Research Corporation, 1996.

[34] Pericleous, K., Cross, M., Moran, G., Chow, P., and Chan, K., "Free surface Navier-Stokes flows with simultaneous heat transfer and solidification/melting," *Advances in Computational Mathematics*, Vol. 6, No. 1, 1996, pp. 295–308.

[35] Barsi, S., and Kassemi, M., *Validation of Tank Self-Pressurization Models in Normal Gravity*, 2007. https://doi.org/10.2514/6.2007-952, URL https://arc.aiaa.org/doi/abs/10.2514/6.2007-952.

[36] Linstrom, P., and Mallard, W., "Editors," *NIST Chemistry WebBook, NIST Std. Ref. Database Number 69, NIST*, 2005. URL http://webbook.nist.gov.